

Creating a Ferromagnetic Ground State with T_c Above Room Temperature in a Paramagnetic Alloy through Non-Equilibrium Nanostructuring

Xinglong Ye,* Nuno Fortunato, Abhishek Sarkar, Holger Geßwein, Di Wang, Xiang Chen, Benedikt Eggert, Heiko Wende, Richard A. Brand, Hongbin Zhang, Horst Hahn, and Robert Kruk*


Materials with strong magnetostructural coupling have complex energy landscapes featuring multiple local ground states, thus making it possible to switch among distinct magnetic-electronic properties. However, these energy minima are rarely accessible by a mere application of an external stimuli to the system in equilibrium state. A ferromagnetic ground state, with T_c above room temperature, can be created in an initially paramagnetic alloy by nonequilibrium nanostructuring. By a dealloying process, bulk chemically disordered FeRh alloys are transformed into a nanoporous structure with the topology of a few nanometer-sized ligaments and nodes. Magnetometry and Mössbauer spectroscopy reveal the coexistence of two magnetic ground states, a conventional low-temperature spin-glass and a hitherto-unknown robust ferromagnetic phase. The emergence of the ferromagnetic phase is validated by density functional theory calculations showing that local tetragonal distortion induced by surface stress favors ferromagnetic ordering. The study provides a means for reaching conventionally inaccessible magnetic states, resulting in a complete on/off ferromagnetic–paramagnetic switching over a broad temperature range.

1. Introduction

Materials with magnetic ordering that strongly couples with crystal structure and lattice distortion often have complex free-energy landscapes with many possible local minima.^[1–3] As a result, the magnetic properties of a ferromagnetic phase can be adjusted near its equilibrium state by external strain. For example, epitaxial strain has been imparted to ferromagnetic thin films through the pre-determined substrate in order to change Curie temperature,^[4–6] magnetization^[7,8] and magnetic anisotropy.^[9] To functionalize materials, the strain can be driven electrically using piezoelectric substrates enabling applications in spintronics and magnetic random access memory.^[10,11] New opportunities arise when entirely different magnetic ground states present in the material's free-energy landscape can be reached by straining. This enables, for example, the

X. Ye, A. Sarkar, D. Wang, H. Hahn, R. Kruk
Institute of Nanotechnology
Karlsruhe Institute of Technology
76344 Eggenstein-Leopoldshafen, Germany
E-mail: xing-long.ye@kit.edu; robert.kruk@kit.edu

N. Fortunato, A. Sarkar, H. Zhang
Institute of Materials Science
Technische Universität Darmstadt
64287 Darmstadt, Germany

 The ORCID identification number(s) for the author(s) of this article can be found under <https://doi.org/10.1002/adma.202108793>.

© 2022 The Authors. Advanced Materials published by Wiley-VCH GmbH. This is an open access article under the terms of the Creative Commons Attribution-NonCommercial License, which permits use, distribution and reproduction in any medium, provided the original work is properly cited and is not used for commercial purposes.

DOI: 10.1002/adma.202108793

H. Geßwein
Institute for Applied Materials
Karlsruhe Institute of Technology
76344 Eggenstein-Leopoldshafen, Germany

D. Wang
Karlsruhe Nano Micro Facility
Karlsruhe Institute of Technology
76131 Karlsruhe, Germany

X. Chen
Nano and Heterogeneous Materials Center
School of Materials Science and Engineering
Nanjing University of Science and Technology
Nanjing 210094, China

B. Eggert, H. Wende, R. A. Brand
Faculty of Physics and Center for Nanointegration Duisburg-Essen (CENIDE)
University of Duisburg-Essen
47057 Duisburg, Germany

on/off switching between ferromagnetism and paramagnetism resulting in a complete change of magnetic properties over a broad temperature range. It has been reported that in perovskite oxides^[12,13] and magnetic semiconductors,^[14] an initially paramagnetic/diamagnetic ground state can be converted into a ferromagnetic ground state by epitaxial strain. However, these newly created ferromagnetic states usually have Curie temperatures far below room temperature and/or small saturation magnetization. In this work, we have used non-equilibrium nanostructuring and resulting strain to create magnetically ordered ground states, especially with high ordering temperatures, from an initially magnetically disordered material.

One candidate material to consider for toggling of magnetic ground states with stress is Fe–Rh alloy, which has strong magnetostructural coupling and consequently features rich free-energy landscape. The chemically ordered $\text{Fe}_{1-x}\text{Rh}_x$ alloy ($0.48 < x < 0.54$) shows an antiferromagnetic (AFM)–ferromagnetic (FM) transition when heated to ≈ 350 K, accompanied by $\approx 1\%$ lattice expansion.^[15–19] The AFM–FM transition is highly sensitive to external stimuli such as pressure,^[20] antisite disorder,^[21] and charge transfer induced by optical excitation.^[22] The AFM–FM transition temperature can be shifted by 25 K by electrically driven strain in FeRh/BaTiO₃ heterostructure.^[23] Moreover, the AFM–FM transition can be suppressed when B2 FeRh is reduced to extremely small sizes (≈ 3 nm), pointing out the critical role of the surface at the nanoscale in stabilizing the ferromagnetic state.^[24,25] On the other hand, chemically disordered FeRh, which usually exist only at high temperatures in a paramagnetic state, has received little attention.^[26–28] However, the presence of a low-temperature spin-glass ground state in nanocrystalline, chemically disordered FeRh points toward a strong competition between AFM and FM interactions.^[29–31] One may expect that by nanostructuring, where surface effects and strain play essential roles, the balance between those competing interactions can be tilted toward the emergence of a magnetically ordered state.

Here, we transformed the chemically disordered fcc FeRh alloy into a nanoporous (NP) structure made of solid struts (ligaments) and nodes by a highly dynamic, non-equilibrium dealloying process. In the dealloying process, the less noble element of an alloy, here Fe atoms, is selectively dissolved, while the noble Rh element with higher electronegativity remains to form a NP structure.^[32–34] The NP structure arises from the spinodal decomposition of the vacancy-adatom solution through uphill diffusion at the alloy/electrolyte interface. This dissolution/surface diffusion process is thus highly dynamic and far away from equilibrium, and can produce extremely small ligaments and nodes in a metastable state. Due to their small size, surface stress can induce very large strain in ligaments and nodes.^[35,36] We have prepared the chemically disordered NP FeRh with ligament and node sizes of only 2–3 nm by the dealloying of FeRh alloys. Furthermore, by changing the dealloying potentials the fraction of the remaining Fe atoms can be tailored, which allows for the control of the composition of the resultant NP structure.^[37] We discovered two magnetic ground states coexist in NP FeRh—an expected low-temperature spin-glass and a hitherto-unknown robust ferromagnetic phase with T_c above room temperature. In the proposed theoretical model, the emergence of the

ferromagnetic ground state can be attributed to the tetragonal strain induced by surface stress in the ligaments as verified by density functional theory calculations.

2. Results and Discussion

2.1. Electrochemical Dealloying and Microstructural Overview of NP FeRh

NP FeRh samples were prepared by the electrochemical dealloying of the $\text{Fe}_{85}\text{Rh}_{15}$ alloy. The pristine alloys were obtained by repetitive arc melting of Fe and Rh wires (with purity $> 99.99\%$) in Ar atmosphere, which were then annealed at 1000 °C under argon atmosphere for four days to ensure composition homogeneity. X-ray diffraction shows the single-phase bcc structure, typical of bulk FeRh alloys at room temperature. We performed the electrochemical dealloying of the $\text{Fe}_{85}\text{Rh}_{15}$ alloy in 1 M H_2SO_4 by applying different potentials to optimize the process. The critical dealloying potential of $\text{Fe}_{85}\text{Rh}_{15}$ was determined to be -0.440 V, above which the dealloying can proceed. Therefore, we used the potentials slightly more positive than -0.440 V to perform the dealloying. **Figure 1A** shows the evolution of the crystal structure of the $\text{Fe}_{85}\text{Rh}_{15}$ alloy at -0.425 V using in situ X-ray diffraction. As the dealloying started, the intensity of the bcc diffraction peaks decreased slowly. Meanwhile, another set of broad diffraction peaks started to appear after ≈ 7 h, which could be indexed with an fcc structure. After about 20 h, the intensity of the newly developed peaks remained unchanged, indicating the completeness of the dealloying process. Rietveld analysis shows that the average micro-strain and grain size that contribute to the peak broadening are around 0.79% and $5(1)$ nm, respectively (**Figure 1B**). The micro-strain is about eight times that obtained in NP-Au ($\approx 0.1\%$) with large ligaments (≈ 37 nm) and can be attributed to the much smaller ligaments in NP FeRh.^[38] Moreover, the relative displacement between 111_{fcc} and 200_{fcc} peaks indicates the presence of stacking faults^[39] and/or anisotropic strain. By including stacking faults into the fitting procedure, its probability was refined to be around 6% (top plot in **Figure 1B**). However, even after accounting for grain size, micro-strain, and stacking faults, there is still some misfit between the measured and simulated XRD patterns, for instance, around the asymmetric 311_{fcc} peak (inset in **Figure 1B**). This suggests that the distortion of the fcc lattice is due to the surface-induced strain. We emphasize that Fe concentrations in NP FeRh can be varied from 65 at% to ≈ 20 at% by changing the dealloying potentials from -0.440 to -0.390 V, and -0.425 V was specifically chosen to obtain a nominal composition of $\text{Fe}_{50}\text{Rh}_{50}$ (**Figure S1**, Supporting Information). All obtained NP samples prepared at different dealloying potentials show the fcc structure rather than the bcc one, verifying the stabilization of the chemically disordered fcc structure in NP FeRh.

We studied the microstructure of NP- $\text{Fe}_{50}\text{Rh}_{50}$ by transmission electron microscopy (TEM). **Figure 1C** shows the typical NP structure consisting of bi-continuous ligaments and pores with sizes of only 2–3 nm (**Figure 1C**). The measured ligament sizes agree with those determined by XRD results. It can be seen that the NP structure can be described by the

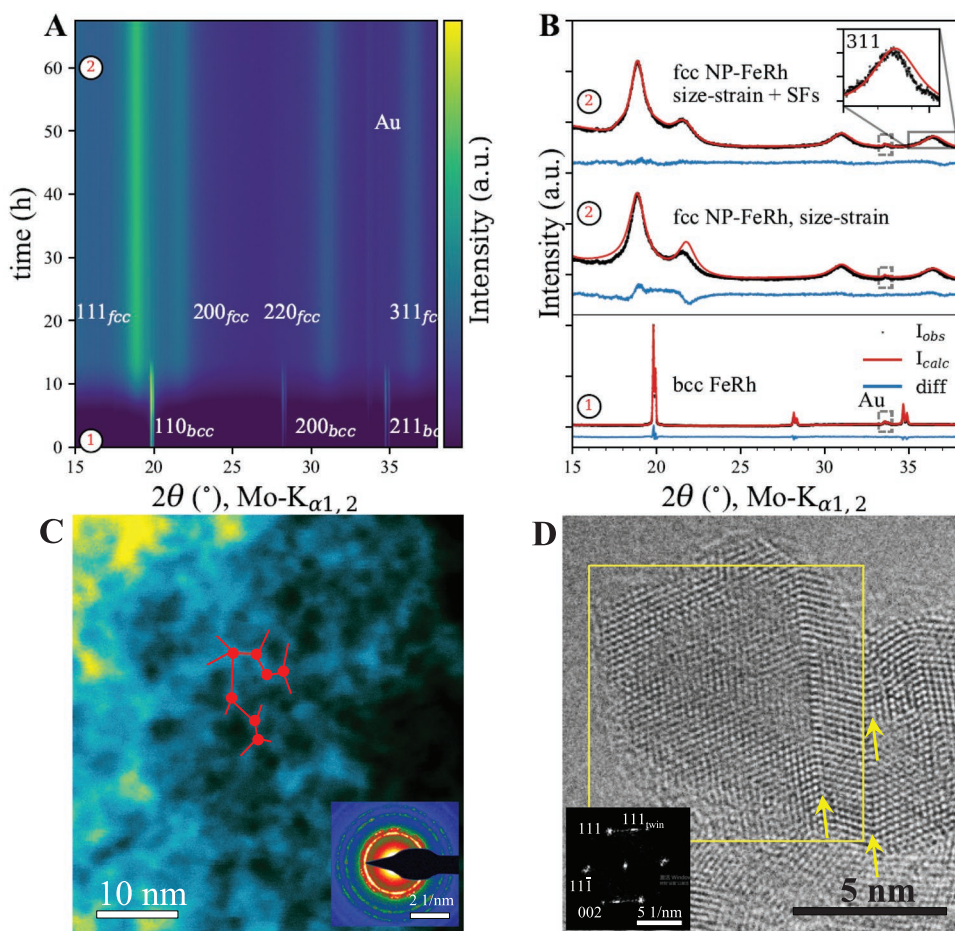


Figure 1. Microstructural overview of the chemically disordered nanoporous $\text{Fe}_{50}\text{Rh}_{50}$. A) Contour plot of in situ X-ray diffraction patterns during the dealloying of $\text{Fe}_{85}\text{Rh}_{15}$ alloy at -0.425 V, showing the bcc to fcc phase transformation. B) Rietveld fitting of the diffraction patterns before (①) and after dealloying (②). Inset shows an enlarged view of the fitting around 311 peak. The Au diffraction arises from the Au wires used for electrically connecting the FeRh sample. C) A bright-field TEM image showing NP structure with characteristic length scale of only 2–3 nm. The ligament-node topology of NP structure is schematically sketched by dashed lines and dots. (Inset) Corresponding selected area diffraction patterns verifying the fcc structure. D) A close-up HRTEM image of a single ligament and its Fourier transformation showing the fcc structure. The yellow arrows indicate twin boundaries.

ligament-node topology, in which the ligaments are connected by the nodes (schematic in Figure 1C). Selected-area electron diffraction (SAED) shows nearly continuous diffraction rings of the fcc structure, indicating randomly oriented nanosized grains. A close-up high-resolution TEM (HRTEM) image of a single ligament shows the lattice fringes originating exclusively from the fcc structure with twin boundaries (Figure 1D). Energy-dispersive spectroscopy (EDS) mapping shows the homogeneous distribution of Fe and Rh atoms with the random composition fluctuation of a few atomic percent. No noticeable phase separation was observed (Figure S2, Supporting Information).

2.2. The Coexistence of Ferromagnetic and Spin-Glass Ground States in NP FeRh

We explored the magnetic properties of NP $\text{Fe}_{50}\text{Rh}_{50}$ by superconducting quantum interference device (SQUID) magnetometry. As shown in Figure 2A, the magnetic hysteresis loops

display the typical ferromagnetic behavior with apparent zero coercivity at 300 and 350 K. When the sample was cooled down to 5 K, the coercivity increased to ≈ 0.1 T. A temperature dependence of coercivity shows that it only starts to appear between 70 and 100 K and then increases with decreasing temperatures (Figure S3, Supporting Information), indicating a superparamagnetic blocking behavior of small ferromagnetic clusters below 100 K. Accordingly, the zero-field-cooled (ZFC) curve exhibits a peak at the blocking temperature of 87 K (referred to as T_b) (Figure 2B). AC susceptibility measurements reveal that T_b shifts to larger values at higher frequencies (Figure 2C). The dependence of the relaxation time ($\tau = 2\pi/f$) on $1/T_b$ follows the Néel–Brown model^[40]

$$\ln \tau = (E_a/kT_b) + \ln \tau_0 \quad (1)$$

with τ_0 being time constant and k the Boltzmann constant. The best linear fit yields the anisotropy energy $E_a = 1.4 \times 10^{-20}$ J and $\tau_0 = 8.6 \times 10^{-10}$ s, confirming the superparamagnetic blocking process and ferromagnetic ordering in NP FeRh (Figure 2D).

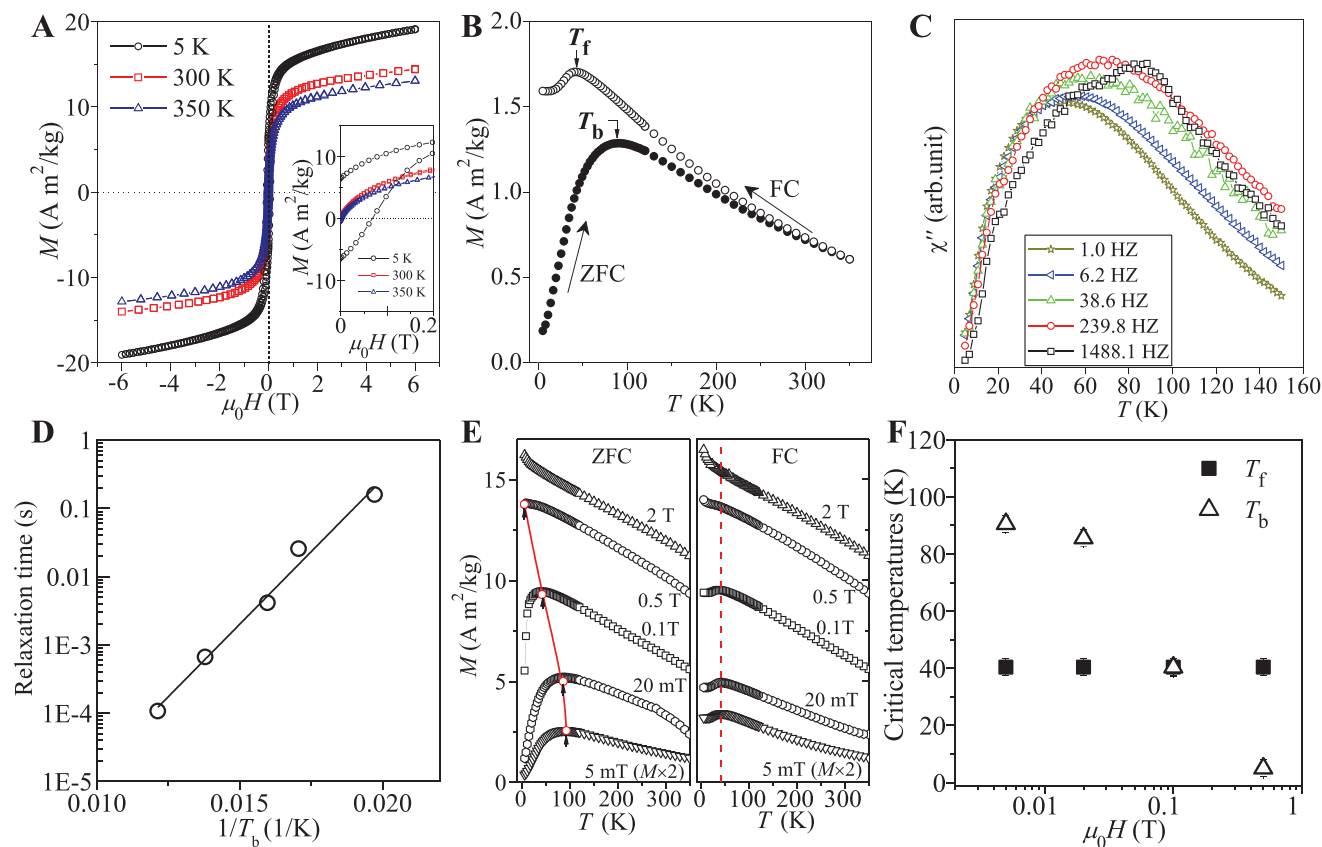


Figure 2. Coexistence of spin-glass and robust ferromagnetic phase in NP Fe₅₀Rh₅₀. A) Magnetic hysteresis loops at 5 K, 300 K, and 350 K, respectively. (Inset) Enlarged view of the 1st and 4th quadrants in low-field regime showing the emergence of the large coercivity at 5 K. B) ZFC and FC magnetization curves under 5 mT, showing the superparamagnetic blocking behavior in ZFC curve and the magnetization cusp in FC curve. C) The temperature dependence of the out-of-phase part of AC susceptibility at different frequencies (f), and D) a semilogarithmic plot of the relaxation time ($2\pi/f$) against $1/T_b$, which follows the Néel–Brown model (linear fit). The applied static and driving fields are 20 and 0.35 mT, respectively. E) The ZFC and FC curves under various magnetic fields and F) the corresponding plots of the T_b and T_f against the applied magnetic fields, showing the decrease of T_b and the invariance of T_f under larger fields.

The field-cooled (FC) magnetization, however, displays another clear cusp at 40 K (referred to as T_f) and levels off at low temperatures (Figure 2B). Since in pure superparamagnetic systems the FC magnetization can only increase with decreasing temperatures, the extra cusp observed in FC curve can only be attributed to another magnetic phase. Usually, the cusp and flattening of the FC magnetization below T_f is a signature of spin-glass freezing.^[41,42] Moreover, we observed the completely different dependence of T_f and T_b on the external fields (Figure 2E). T_b decreases from 90 K at 5 mT to below 5 K at 0.5 T (Figure 2F). This is due to the reduced anisotropic energy barrier under magnetic field (E_a in Equation 1). In contrast, T_f stays constant at 40 K from 50 mT to 0.1 T. At 0.5 T, the cusp in FC curve disappears, and the magnetization exhibits a kink at 40 K. At 2 T, the magnetization increases sharply at 40 K (Figure 2E). This independence of T_f of the applied magnetic fields indicates a magnetic transition from a paramagnetic to a spin-glass state below T_f (40 K). When cooled below T_f , the spins from the paramagnetic state freeze in random directions, reducing the magnetization. When the external magnetic field is large enough, the frozen spins are forced to rotate toward the field, which increases the magnetization

sharply (Figure 2E). It is worthwhile to note that a magnetization cusp usually also exists in the ZFC curve in a spin glass.^[41,42] However, NP FeRh consists of both a spin-glass and a ferromagnetic/superparamagnetic phase. In this particular case, the T_b of superparamagnetic phase is higher than the T_f of spin-glass phase. Consequently, the ZFC spin-glass cusp is obscured by the much stronger increase of magnetization due to the de-blocking of ferromagnetic clusters. Altogether, the magnetometry results suggest the coexistence of two magnetic ground states, with T_b and T_f originating respectively from superparamagnetic blocking of ferromagnetic phases and the freezing of spin-glass phase.

Further, Mössbauer spectroscopy was used to cross-check the coexistence of the two magnetic phases. The site-specificity of Mössbauer spectroscopy reveals the Fe local magnetic environments in the spin-glass and ferromagnetic phases through the hyperfine field (B_{hf}) at the ⁵⁷Fe nuclei. Each Fe atom belonging to one of the magnetic phases contributes a set of six absorption peaks (magnetic sextets) to the Mössbauer spectrum. The splitting of the magnetic sextet is proportional to B_{hf} , which is different for the two magnetic phases and thus enables their identification. **Figure 3A** shows that the spectrum at 13 K has

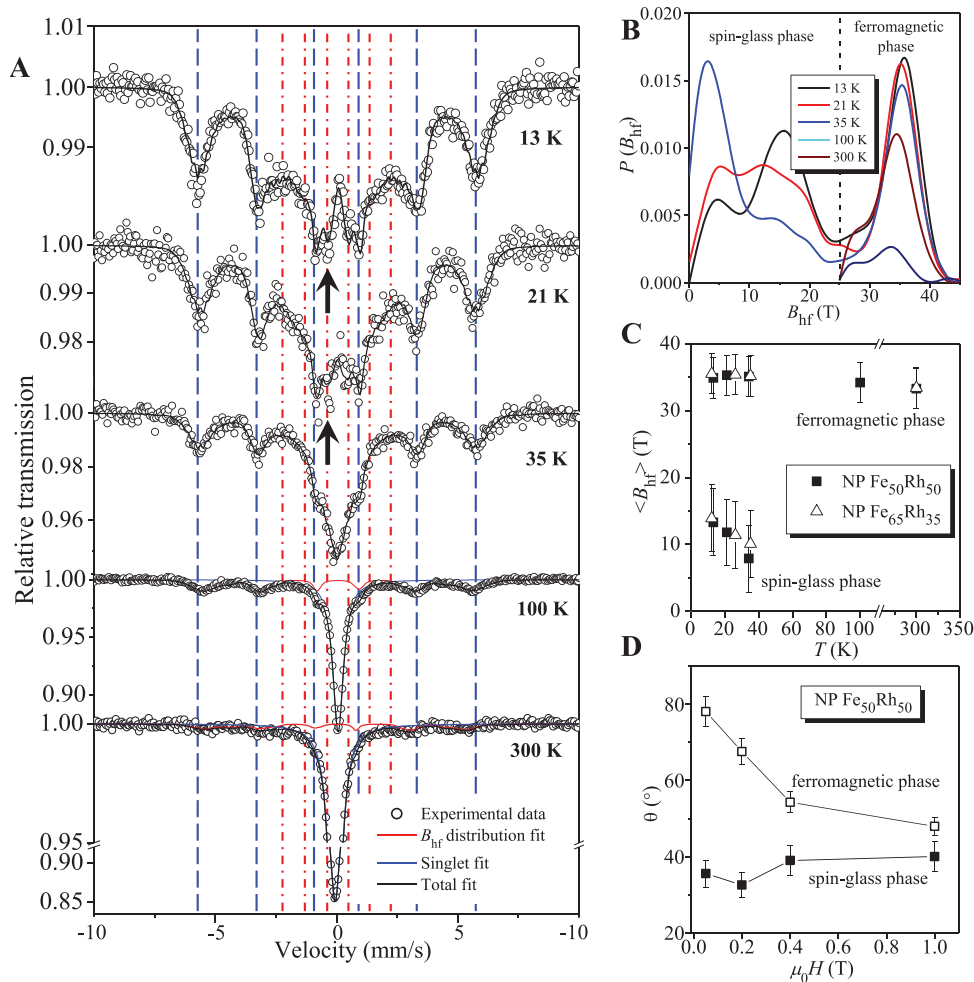


Figure 3. Site-specific Mössbauer spectra of NP Fe₅₀Rh₅₀ at different temperatures. A) Experimental spectra (black circles) at different temperatures and their best fitting using the distribution of hyperfine fields (B_{hf}) and the paramagnetic singlet (only for 100 and 300 K). B) The corresponding B_{hf} distribution consisting of two clearly separated broad parts, with the low-field part corresponding to the spin-glass phase (marked by the red dashed-dotted lines) and the high-field part corresponding to ferromagnetic phase (marked by the blue dashed lines). The black arrows in (A) denote the 3rd line of the spin-glass phase. C) The temperature dependence of the averaged $\langle B_{\text{hf}} \rangle$ in the ferromagnetic and spin-glass phases. Note that the $\langle B_{\text{hf}} \rangle$ values of the ferromagnetic phase remain nearly constant at ≈ 34 T up to 300 K, and that the $\langle B_{\text{hf}} \rangle$ values of the spin-glass phase decrease drastically with increasing temperature and drop to zero values at 35 K. The $\langle B_{\text{hf}} \rangle$ of NP Fe₆₅Rh₃₅ is also included for comparison. D) The field dependence of the angle $\langle \theta \rangle$ between the γ -rays and local Fe spins obtained from in-field Mössbauer spectra. The $\langle \theta \rangle$ in the ferromagnetic phase decreases sharply under higher magnetic fields while that of the spin-glass phase remains constant.

broad absorption peaks, indicating a broad distribution of B_{hf} . As shown in Figure 3B, the corresponding B_{hf} distribution clearly consists of two parts—one high-field part located at ≈ 34 T and another low-field part at ≈ 11 T. These two parts are ascribed to the outer sextet (marked by purple lines) and the inner sextet (marked by red lines, only the 3rd and 4th lines visible as indicated by red arrows) in Figure 3A. The consequent assignment of the two Mössbauer sub-spectra to the two magnetic phases can be realized by analyzing their temperature evolution. At 21 K, the Mössbauer spectrum remains unchanged. However, when the temperature was raised to 35 K, which is close to T_f , the 3rd and 4th lines of the inner sextet disappear and a singlet emerges at the center (Figure 3A). Accordingly, the low-field part of the B_{hf} distribution shifts to near zero value (Figure 3B). This observation indicates the magnetic transition

from a spin-glass to a paramagnetic state at 35 K, consistent with the magnetometry results (Figure 2). In contrast, the intensity of the ferromagnetic sextet remains unchanged at 35 K and only starts to decrease from 100 K, close to the blocking temperature (T_B). At 300 K, the intensity of the ferromagnetic sextet decreases significantly due to the superparamagnetic transition. It should be noted that at 300 K both the spin-glass phase and the superparamagnetic phase contribute to the intensity of the singlet peak.

The ferromagnetic phase and the spin-glass phase can be clearly demonstrated by the temperature dependence of their averaged hyperfine field $\langle B_{\text{hf}} \rangle$, which are calculated from the B_{hf} distribution by $\langle B_{\text{hf}} \rangle = \int B_{\text{hf}} P(B_{\text{hf}}) dB_{\text{hf}} / \int P(B_{\text{hf}}) dB_{\text{hf}}$ in respective regions (Figure 3B). Figure 3C shows that the $\langle B_{\text{hf}} \rangle$ of ferromagnetic phase remains nearly constant (≈ 35 T) across

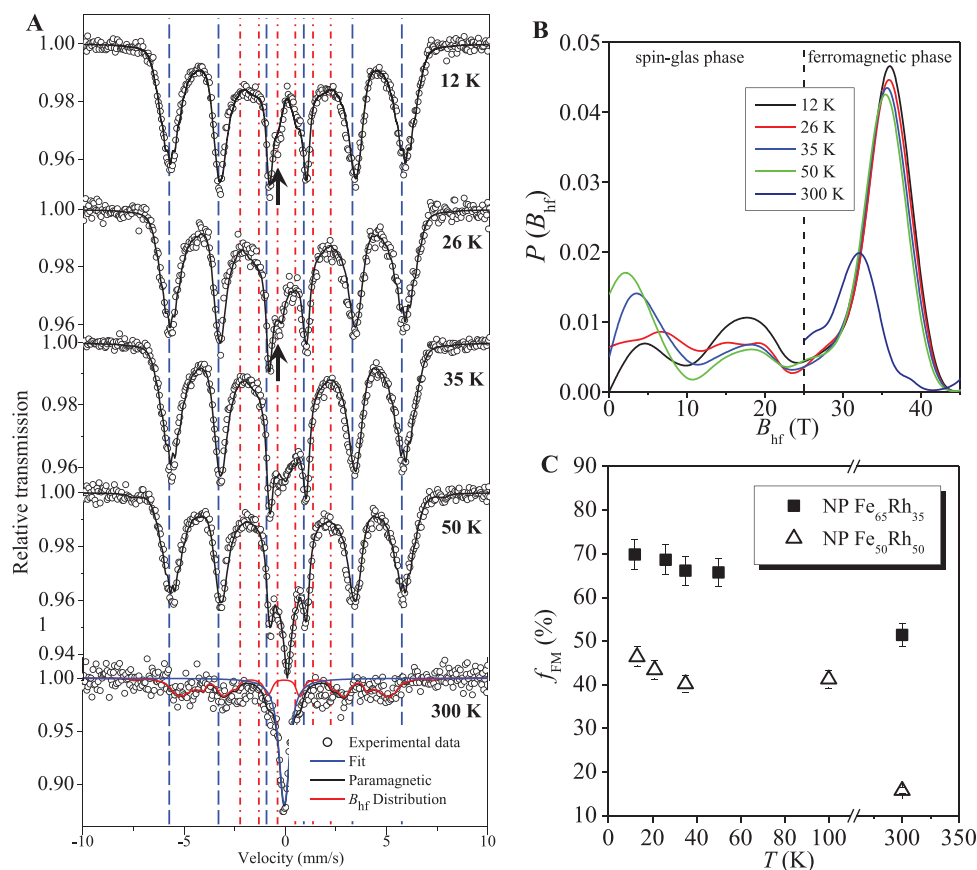


Figure 4. Site-specific Mössbauer spectra of NP Fe₆₅Rh₃₅ at different temperatures. A) Experimental spectra (black circles) at different temperatures and their best fitting using the distribution of hyperfine field (B_{hf}) and a paramagnetic singlet. B) The corresponding B_{hf} distribution consisting of two separated broad parts, which are ascribed to the spin-glass (marked by the red dash-dotted lines) and the ferromagnetic phase (marked by the blue dashed lines), respectively. The black arrows in (A) denote the 3rd line of the spin-glass phase. C) The fraction of ferromagnetic phase in NP Fe₆₅Rh₃₅ and Fe₅₀Rh₅₀ at different temperatures.

the whole temperature range to 300 K, evidencing the robust ferromagnetic ordering. On the contrary, the $\langle B_{\text{hf}} \rangle$ of the spin glass decreases sharply at low temperatures and disappears at 35 K, evidencing the magnetic transition to the paramagnetic state.

The actual spin configurations of these two phases were analyzed by in-field Mössbauer spectroscopy (Figure S4, Supporting Information). The Mössbauer spectroscopy carried out in the external field allows for extracting information about the Fe spin orientations with respect to the γ -rays and external field directions. The average angle θ between local Fe spins and incident γ -rays is described by $\cos^2\theta = (4 - A_{23})/(4 + A_{23})$ with A_{23} being the line intensity ratio (I_2/I_3). Thus, A_{23} has extreme values of 0 and 4 for $\theta = 0^\circ$ and 90° , and an isotropic distribution of local spins yields an effective θ of ca. 54° . Figure 3D shows that under 50 mT the ferromagnetic phase exhibits the angle $\theta \approx 78^\circ$. This indicates a preferential in-plane spin alignment due to the dominant shape anisotropy in NP FeRh with a thin-sheet shape (Figure S1, Supporting Information), again confirming the ferromagnetic ordering. Under higher fields, the angle decreases drastically as the spins of ferromagnetic phase rotates toward the external field. By contrast,

the spin-glass phase shows a preferred out-of-plane orientation ($\theta \approx 38^\circ$) at 50 mT, matching the results observed in other spin glasses.^[43] Furthermore, the spin direction is resistant to larger magnetic fields and stays at around 40° , reflecting the rigidity of frozen spins in the spin glass. Thus, the magnetometry and Mössbauer results consistently reveal the coexistence of the spin-glass and ferromagnetic ground states in chemically disordered NP FeRh.

The coexistence of the spin-glass and ferromagnetic phases has also been observed in NP FeRh with high Fe concentrations of 65 at%. At 13 K, Mössbauer spectroscopy of NP Fe₆₅Rh₃₅ shows the well-developed magnetic sextet with higher intensity compared with NP Fe₅₀Rh₅₀ (Figure 4A). The corresponding B_{hf} distribution consists of two separated parts, one located at ≈ 35 T and another part at ≈ 13 T, which resemble those observed in NP Fe₅₀Rh₅₀ (Figure 4B). When heated to 35 K, a singlet appears at the center of the spectrum, and the lower part of B_{hf} distribution shifts to near zero value (Figure 4A). This again confirms the spin-glass–paramagnetic transition. In contrast, the intensity of the ferromagnetic sextet remains almost unchanged at 35 K. Further increasing the temperature to 300 K reduces the intensity of ferromagnetic sextet. Noticeably, NP Fe₆₅Rh₃₅ has a much larger fraction of ferromagnetic phase

(69%) than in NP Fe₅₀Rh₅₀ (45%) as summarized in Figure 4C. Figure 3C, compares the $\langle B_{\text{hf}} \rangle$ values of NP Fe₆₅Rh₃₅ and NP Fe₅₀Rh₅₀, which exhibit almost the same values and the temperature dependence.

The combined magnetometry and Mössbauer results reveal the emergence of the ferromagnetic ground state in the chemically disordered fcc NP FeRh. When the temperature is below T_b , NP FeRh exhibits the ferromagnetic behavior with the large coercivity in hysteresis loops and clear magnetic sextets in Mössbauer spectrum. Above T_b , the ferromagnetic phase turns into superparamagnetic state due to extremely small ligament sizes. To estimate the lower range of the Curie temperature, we take into consideration that the superparamagnetic state is a result of the collective fluctuations of the ferromagnetically ordered single domains and can only occur below the bulk Curie temperature (for the same composition). The presence of the superparamagnetic state at 350 K (Figure 2A) thus indicates that the Curie temperature of the ferromagnetic ground state is above room temperature. In addition, the saturation magnetization of NP Fe₅₀Rh₅₀ at 6 T decreases monotonically from 5 to 390 K without any indication of the transition to the paramagnetic state, further confirming the Curie temperature above room temperature (Figure S5, Supporting Information). It is worth noting that the ferromagnetic phase can actually be stabilized at room temperature as seen for the NP Fe₆₅Rh₃₅ where the ferromagnetic sextet is clearly visible at 300 K (Figure 4A).

2.3. DFT Calculations Revealing the Effect of Strain on Magnetic Ground States

The identified spin-glass phase can be interpreted as that observed in bulk nanocrystalline fcc FeRh prepared by rapid quenching^[29] and ball milling.^[30,31] Those materials show almost the same B_{hf} distribution, with $\langle B_{\text{hf}} \rangle$ decreasing from 18 T at 26 at% Fe to 10 T at 65 at% Fe.^[30] The large range of B_{hf} distribution is attributed to the different numbers of the nearest Fe neighbors surrounding ⁵⁷Fe. However, no ferromagnetic phase in these materials has been detected so far. To evaluate the influence of the Fe composition on $\langle B_{\text{hf}} \rangle$ in the spin glass, we performed density functional theory (DFT) calculations using the spin-polarized relativistic Korringa–Kohn–Rostoker (SPR-KKR) method.^[44,45] A spin glass lacks translational symmetry and long-range periodic ordering. It has a myriad of nearly degenerate magnetic ground states, posing challenges for ab initio description of its spin configuration. Thus, we focused on incorporating the vanishing Rh moment in the description of band structure and approximated the random spin orientation by the disordered local moment (DLM) model, wherein each site of the fcc structure is occupied concurrently with collinear spin-up and spin-down Fe atoms.^[46] Figure 5A shows that the calculated B_{hf} values decrease from 20 to 10 T with increasing Fe concentrations, which matches the measured $\langle B_{\text{hf}} \rangle$ in our NP FeRh and the large range of B_{hf} distribution. More importantly, the largest B_{hf} in the spin glass can only

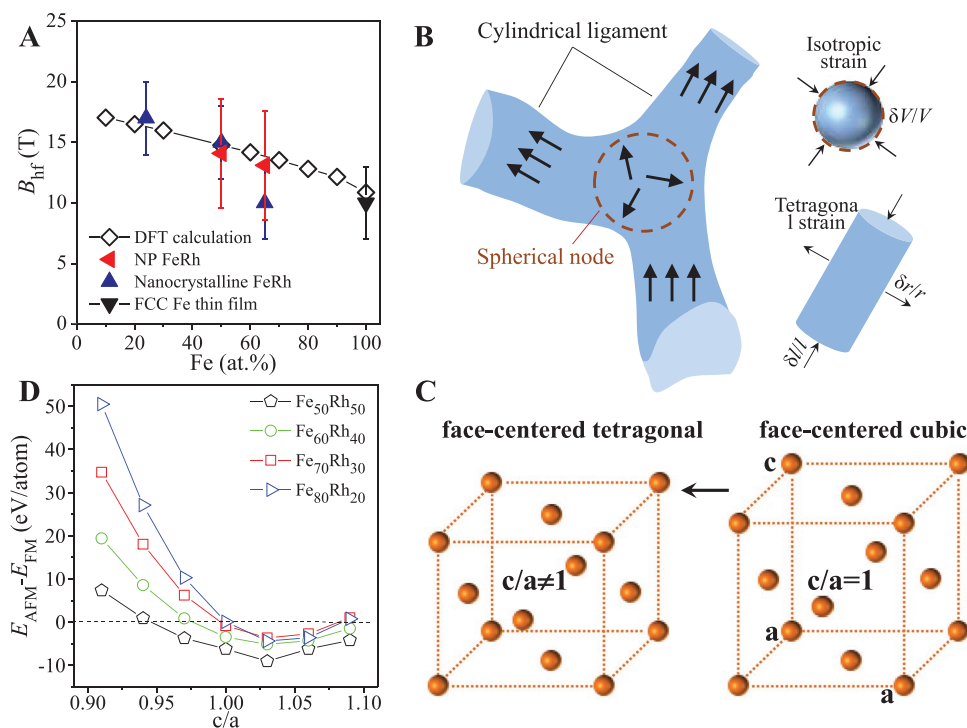


Figure 5. Effect of tetragonal strain on the emergence of ferromagnetic ordering from the spin-glass state by DFT calculations. A) The calculated B_{hf} as a function of Fe concentrations in the spin-glass phase. For comparison, the $\langle B_{\text{hf}} \rangle$ values of NP FeRh, nanocrystalline FeRh and γ -Fe are included. B) Schematic illustration of the different strain states in the ligament-node topology of NP structure. Surface stress induces respective anisotropic strain and isotropic strain in the ligaments and nodes due to their different shapes. C) Illustration of the fcc structure and its tetragonal distortion due to the anisotropic strain in the ligaments. D) The effect of the tetragonal distortion on the competing antiferromagnetic and ferromagnetic states, showing the favored ferromagnetic coupling by tetragonal distortion.

reach up to ≈ 20 T, which corresponds to the extremely dilute Fe atoms embedded in Rh matrix. On the other hand, bulk fcc Fe is paramagnetic with the low B_{hf} below 10 T.^[47,48] In addition, no noticeable element segregation and phase separation were observed (Figure S2, Supporting Information). Hence, the element segregation cannot be regarded as the origin of the ferromagnetic phase with its characteristic hyperfine field of 34 T.

The emergence of the ferromagnetic ground state in NP FeRh rather than in bulk nanocrystalline FeRh points to the decisive role of the surface in changing the magnetic ground state of FeRh. As shown by XRD data, there exists a large strain and lattice distortion in NP FeRh. According to a generalized capillary equation, surface stress can induce a large stress inside a solid by $\langle \Delta P \rangle_v = (2/3)\alpha \langle f \rangle_s$ where ΔP is the hydrostatic component of the stress tensor and f is the scalar surface stress ($1/2 \text{ tr } f$) and α the surface-to-volume ratio.^[35,36] Consequently, the surface stress-induced internal stress and strain in NP metals can be significant due to the extremely large surface-to-volume ratio, as evidenced by spontaneous dimensional change^[49] and tension–compression asymmetry^[50] in NP metals. Most importantly, the strain becomes anisotropic when the shape of a solid is not spherical.^[38,39] For a cylindrical shape, the anisotropic strains are

$$\frac{\delta l}{l} = \frac{\nu - 1}{Y} \alpha f \text{ and } \frac{\delta r}{r} = \frac{3\nu - 1}{2Y} \alpha f \quad (2)$$

along the axial and radial directions, respectively, in which ν is the Poisson's ratio and Y the Young's modulus. As denoted in Figure 1C and schematically illustrated in Figure 5B, the NP structure can be approximated by a topology of cylindrical ligaments connected by spherical nodes.^[51] Continuum mechanics predicts that the nodes experience an isotropic strain, whereas the elongated ligaments an anisotropic strain, which would lead to a tetragonal distortion of the fcc structure in NP FeRh (Figure 5C).^[36] Yet, due to significant peak broadening and the overlapping grains associated with extremely small ligaments, it is challenging to accurately measure the tetragonal distortion in NP FeRh from XRD and TEM results although the asymmetric 311_{fcc} peak suggests its existence (Figure 1A,B). However, in NP Au with large ligaments (≈ 20 nm), local detection technique such as nanobeam diffraction directly observed the tetragonal distortion ($|(c/a) - 1|$) with a value of $\approx 5\%$.^[52] Hence, the theoretical analysis and the experimental results both indicate the surface-induced tetragonal distortion and isotropic strain in the ligaments and nodes of NP-FeRh, respectively, which may account for the coexistence of two magnetic ground states.

Generally, in spin glasses the strong competition between AFM and FM exchange interactions is essential for the frustration of exchange interactions. To probe the origin of the ferromagnetic ground state, we thus calculated the energy difference between the AFM and FM states by DFT as a function of strain, based on AFM γ -Fe.^[53] Figure 5D shows that the energy of AFM state is slightly smaller than that of FM state, verifying the AFM ground state. However, the energy differences are very small, only ≈ 6 meV per atom in $\text{Fe}_{50}\text{Rh}_{50}$, which testifies to the strong competition between AFM and FM interactions. The strong AFM–FM competition, together with the disordered occupation of Fe sites in the fcc lattice, another

essential ingredient of a spin glass, induces the frustration of spin ordering as usually observed in other spin glasses.^[41,54] However, the energy difference becomes smaller when tetragonal distortion is exerted, which eventually favors ferromagnetic ordering and triggers the spin-glass–ferromagnetism transition. Moreover, for higher Fe composition, a smaller tetragonal distortion is required for inducing the magnetic transition. This agrees with the larger fraction of ferromagnetic phase in NP $\text{Fe}_{65}\text{Rh}_{35}$ compared to NP $\text{Fe}_{50}\text{Rh}_{50}$ (Figure 4C). On the contrary, under isotropic strain the energy of AFM state is always smaller than that of ferromagnetic state, and thereby the spin-glass state remains unchanged (Figure S6, Supporting Information). Therefore, the DFT results show that the tetragonal distortion in the ligaments induces the ferromagnetism, whereas the nodes with isotropic strain retains the spin-glass state as in nanocrystalline FeRh prepared by rapid quenching^[29] and ball-milling.^[30,31] Consequently, the ferromagnetic ligaments are decoupled by the spin-glass nodes, explaining why NP FeRh as a bulk sample exhibits superparamagnetism. It is interesting to note that the tetragonal distortion-induced ferromagnetic phase is analogous to that observed in ultrathin γ -Fe film deposited on Cu and Cu–Au substrate. Its magnetic states transforms from the bulk-like AFM state to the ferromagnetic state as the film is expanded in plane by the substrate.^[47,48]

3. Conclusion

We stabilized the chemically disordered fcc FeRh in a nanoporous structure with a topology of a few nanometer-sized ligaments and nodes by a highly dynamic, non-equilibrium dealloying process. The combined structural, magnetometry and Mössbauer spectroscopy studies reveal the emergence of a previously unknown robust ferromagnetic phase with T_c above room temperature as opposed to the conventional low-temperature spin glass. A model, supported by the DFT calculations, is proposed where the ferromagnetic ground state originates from the surface stress-induced tetragonal distortion in the elongated ligaments. This distortion favors the ferromagnetic rather than antiferromagnetic coupling among the local Fe spins. Our study thus demonstrates that a ferromagnetic ground state with T_c well above room temperature can be created from an initially magnetically disordered one. From the practical point of view, this ability to switch between the two distinct magnetic ground states by anisotropic strain will enable a complete control of magnetic properties over a wide temperature range. These findings may inspire further search for, so far, hidden magnetic phases in magnetic materials with strong magnetostructural coupling. In nanoporous FeRh, the ferromagnetic ground state turns into superparamagnetic state above blocking temperatures due to the extremely small ligaments/nodes. To utilize and stabilize the newly discovered ferromagnetism at room temperature, novel composite devices may be envisioned based on the heterostructure consisting of chemically disordered FeRh thin film and a pre-determined substrate that provides the tetragonal distortion. For instance, a complete ferromagnetic–paramagnetic transition may be induced by the voltage-driven strain when combined with a piezoelectric substrate.

4. Experimental Section

Preparation of Nanoporous FeRh and the Electrochemical Setup: Parent alloys with nominal composition of Fe₈₅Rh₁₅ (with atomic percentage) were prepared by repetitive arc melting of Fe and Rh wires (with purity > 99.99%) in Ar atmosphere. The alloy ingots were homogenized at 850 °C for 4 days in quartz tube filled with argon. Then, the alloy ingot was compressed, rolled into thin sheets with a thickness of ≈0.2 mm and cut into millimeter-sized samples. All samples were annealed at 850 °C for 1 h for the recovery prior to dealloying. Electrochemical dealloying was carried out in 1 M H₂SO₄ in a three-electrode electrochemical cell under potentiostatic control (AUTOLAB PGSTAT302N). The working, counter, and reference electrodes were the Fe₈₅Rh₁₅ alloy, the Pt wires and a pseudo Ag/AgCl electrode, respectively. The potential of the pseudo Ag/AgCl electrode is 0.300 ± 0.002 V more positive than the standard Hg/HgO (1 M KOH) electrode, and for comparison, all the voltages in the paper were converted to the Hg/HgO scale. Sulfuric acid with guaranteed reagent grade (Sigma-Aldrich) and ultrapure water with a resistance of 18.2 MΩ (Milli Q Advantage A10) were used for the preparation of the electrolyte solutions.

Linear anodic polarization was first performed to identify the potential where the anodic current starts to rise exponentially and then chronoamperometric measurements were performed to precisely determine the critical dealloying potential, only above which the dealloying can continue. To control the composition of the as-dealloyed nanoporous FeRh, the dealloying potentials of −0.440 V (just 3 mV above the critical dealloying potential), −0.430, −0.425, −0.410, −0.390, and −0.20 V were used for the dealloying. Note that the as-prepared nanoporous FeRh was extremely prone to the oxidation, and it burned within one minutes when exposed to the air. Therefore, the as-prepared nanoporous FeRh samples were cleaned and kept in a dilute H₂SO₄ before microstructural characterization.

In Situ XRD Measurements and Microstructure Characterization: The crystal structure of the Fe₈₅Rh₁₅ alloy during the electrochemical dealloying was monitored using in situ XRD with a parallel beam laboratory rotating anode diffractometer (Mo Kα_{1,2} radiation) in transmission geometry. The transmission geometry allows the detection of the entire volume of the sample (thickness ≈ 0.1 mm). In this setup, the Fe₈₅Rh₁₅ alloy, as the working electrode, was wired by gold wires and attached to a glass plate (thickness ≈ 0.1 mm), which was later immersed in the 1 M H₂SO₄ electrolyte in plastic bags. The counter and reference electrodes were the Pt wire and the pseudo Ag/AgCl electrode, respectively. Diffraction patterns were collected every 10 min with a Pilatus 300K-W area detector. The standard reference material NIST SRM660b LaB₆ powder was used for the detector calibration and the determination of the instrumental resolution. The 2D diffraction images were integrated using the pyFAI^[55] software and analyzed with the Rietveld method (TOPAS V6). An isotropic size-strain model based on a double-Voigt approach was used to describe the line broadening. Due to the discrepancy of describing the diffraction profiles of the 111_{fcc} and 200_{fcc} peaks, the microstructural structural model was extended to account for the existence stacking disorder.^[36] This model is based on DIFFaX like simulations of different stacking sequences describing different types of microstructural features like intrinsic stacking faults and twinning and adapted from ref. [56] implemented in TOPAS macro language.

The microstructure of the as-prepared sample was characterized using a field-emission scanning electron microscope equipped with energy-dispersive X-ray spectroscopy (Zeiss Ultra 600), and using a transmission electron microscope (FEI Titan 80-300) with EDS. In order to avoid oxidation during sample transfer, the as-prepared sample was transferred into the scanning electron microscope chamber immediately after moved out from the dilute H₂SO₄ electrolyte for scanning electron microscopy (SEM) observation. At least 30 different positions under SEM were measured to get an average of the composition.

For the preparation of the TEM samples, the as-prepared samples were transferred into the glove box and ground to fine powders. A small amount of powders were then attached to a Cu grid covered with carbon

film for further TEM observations. Afterward, the Cu grid was mounted to the TEM sample holder, and then transferred to TEM for further characterization using a vacuum transfer hold (Themis 300). Each data of mean ligament size was obtained by measuring at least 30 individual ligaments. EDS mapping was used to examine the distribution of Fe and Rh in the ligaments, and the size resolution is less than 2 nm.

Magnetometry and Mössbauer Measurements: Magnetic measurements were performed in a superconducting quantum interference device (SQUID, MPMS3) with applied magnetic field parallel to the surface of the as-prepared nanoporous samples. Temperature dependent magnetization measurements were performed following the usual zero-field cooled (ZFC) and field-cooled (FC) protocols: the sample was first cooled down from 350 to 5 K in zero magnetic field, and then a static magnetic field was applied. During warming up from 5 to 350 K the ZFC magnetization was measured, and FC magnetization was measured during further cooling down from 350 to 5 K. Alternating current (AC) susceptibility measurements were performed in the frequency range from ≈1 to 1000 Hz as a function of temperatures near the peak temperature in ZFC curve. The applied static field is 0.2 mT, and the driving field is 0.35 mT.

To gain insight into the magnetic environment of the ⁵⁷Fe atoms, Mössbauer spectra with a ⁵⁷Co:Rh source were acquired in transmission geometry at various temperatures using a triangular sweep of the velocity scale. Zero-field spectra were measured at KIT, and in-field spectra were collected at Universität Duisburg-Essen. The incidence of the γ-rays was perpendicular to the sample surface, and during the measurements, the samples were protected under He. The velocity of the spectrometer was calibrated with a α-Fe foil reference sample at room temperature. The effective thickness of the nanoporous FeRh was optimized to improve the absorption line resolution (10–20 mg cm^{−2}). The Mössbauer patterns were simulated by superimposing 40 elementary Lorentzian sextets with 0.30 mm line width, which covers a range of 60 T. Each point in the probability distribution was assumed to be proportional to the relative intensity of the corresponding sextet.

DFT Calculations: To rationalize the coexistence of the spin-glass phase and robust ferromagnetic phase within the same fcc phase structure we performed density functional theory (DFT) calculations using the spin polarized relativistic KKR (SPR-KKR) program.^[41] The chemical disorder is treated within the coherent potential approximation,^[57] and we adopted a scalar-relativistic spin-polarized approach and the Perdew–Burke–Ernzerhof (PBE) function.^[45] The angular-moment cut-off was set to *l* = 3 and the convergence testing showed little dependence of *B*_{hf} on higher cut-off values. For the hyperfine calculations we adopted a *k*-point density of NKTAB = 4000 to ensure good convergence and 450 was used when finding the volume minima of each structure. To describe the absence of long-range magnetic ordering, we employed the disordered local moment (DLM) approach.^[46] The DLM state consists of atomic sites occupied with two Fe species, one with spin up and another with spin down, thus describing a paramagnetic or spin-glass state. To elucidate the origin of robust ferromagnetic ordering in nanoporous FeRh NPs, we examined the competing AFM and FM interactions in fcc FeRh. To that end, we compared the energies of the FM and AFM states, based on the AFM ground state of fcc Fe^[53] as a function of volume and tetragonal strain at different compositions.

Supporting Information

Supporting Information is available from the Wiley Online Library or from the author.

Acknowledgements

The authors thank T.T.R. for the assistance in AC susceptibility measurements. The authors appreciate financial support from Deutsche Forschungsgemeinschaft under contract number HA 1344/34-1 (R.K, H.H.)

as well as the OCPC-Helmholtz program and Alexander von Humboldt Foundation (X.Y.). B.E, H.W., and H.Z. acknowledge the financial support from the Deutsche Forschungsgemeinschaft within the Collaborative Research Centre / Transregio (CRC/TRR) 270 (Project-ID 405553726, projects A05 and B05). N.F. and H.Z. acknowledge the financial support by the European Research Council (ERC) under the European Union's Horizon 2020 research and innovation programme (grant no. 743116 - project "Cool Innov"). The Lichtenberg high-performance computer of the TU Darmstadt and KNMF are acknowledged.

Open access funding enabled and organized by Projekt DEAL.

Conflict of Interest

The authors declare no conflict of interest.

Author Contributions

X.Y., R.K., and H.H. conceived the project. X.Y. designed and performed the experiments. N.F. and H.Z. conducted DFT calculations and analysis. H.G. and X.Y. performed in situ XRD; D.W. and X.C. performed TEM observation. A.S. and B.E. conducted Mössbauer measurements, and R.B. contributed to the interpretation of results. X.Y. wrote the draft and all authors participated in the discussions, improved the manuscript and approved the submitted manuscript.

Data Availability Statement

The data that support the findings of this study are available from the corresponding author upon reasonable request.

Keywords

FeRh alloys, ferromagnetic materials, magnetostructural coupling, multiple ground states, non-equilibrium nanostructuring, paramagnetic materials

Received: November 1, 2021

Revised: November 24, 2021

Published online:

- [1] J. Wang, *Annu. Rev. Mater. Res.* **2019**, *49*, 361.
- [2] R. Ramesh, D. G. Schlom, *Nat. Rev. Mater.* **2019**, *4*, 257.
- [3] J. Ma, J. Hu, Z. Li, C.-W. Nan, *Adv. Mater.* **2011**, *23*, 1062.
- [4] R. S. Beach, J. A. Borchers, A. Matheny, R. W. Erwin, M. B. Salamon, B. Everitt, K. Pettit, J. J. Rhyne, C. P. Flynn, *Phys. Rev. Lett.* **1993**, *70*, 3502.
- [5] J. H. Haeni, P. Irvin, W. Chang, R. Uecker, P. Reiche, Y. L. Li, S. Choudhury, W. Tian, M. E. Hawley, B. Craigo, A. K. Tagantsev, X. Q. Pan, S. K. Streiffer, L. Q. Chen, S. W. Kirchoefer, J. Levy, D. G. Schlom, *Nature* **2004**, *430*, 758.
- [6] Y. Yokoyama, Y. Yamasaki, M. Taguchi, Y. Hirata, K. Takubo, J. Miyawaki, Y. Harada, D. Asakura, J. Fujioka, M. Nakamura, H. Daimon, M. Kawasaki, Y. Tokura, H. Wadati, *Phys. Rev. Lett.* **2018**, *120*, 206402.
- [7] X. Moya, L. E. Hueso, F. Maccherozzi, A. I. Tovstolytkin, D. I. Podyalovskii, C. Ducati, L. C. Phillips, M. Ghidini, O. Hovorka, A. Berger, M. E. Vickers, E. Defay, S. S. Dhessi, N. D. Mathur, *Nat. Mater.* **2013**, *12*, 52.
- [8] C. Thiele, K. Dörr, O. Bilani, J. Rödel, L. Schultz, *Phys. Rev. B* **2007**, *75*, 054408.
- [9] C. Du, R. Adur, H. Wang, A. J. Hauser, F. Yang, P. C. Hammel, *Phys. Rev. Lett.* **2013**, *110*, 147204.
- [10] S. Zhang, Y. G. Zhao, P. S. Li, J. J. Yang, S. Rizwan, J. X. Zhang, J. Seidel, T. L. Qu, Y. J. Yang, Z. L. Luo, Q. He, T. Zou, Q. P. Chen, J. W. Wang, L. F. Yang, Y. Sun, Y. Z. Wu, X. Xiao, X. F. Jin, J. Huang, C. Gao, X. F. Han, R. Ramesh, *Phys. Rev. Lett.* **2012**, *108*, 137203.
- [11] W. Eerenstein, M. Wiora, J. L. Prieto, J. F. Scott, N. D. Mathur, *Nat. Mater.* **2007**, *6*, 348.
- [12] J. H. Lee, L. Fang, E. Vlahos, X. Ke, Y. W. Jung, L. F. Kourkoutis, J.-W. Kim, P. J. Ryan, T. Heeg, M. Roeckerath, V. Goian, M. Bernhagen, R. Uecker, P. C. Hammel, K. M. Rabe, S. Kamba, J. Schubert, J. W. Freeland, D. A. Muller, C. J. Fennie, P. Schiffer, V. Gopalan, E. Johnston-Halperin, D. G. Schlom, *Nature* **2010**, *466*, 954.
- [13] D. Fuchs, C. Pinta, T. Schwarz, P. Schweiss, P. Nagel, S. Schuppler, R. Schneider, M. Merz, G. Roth, H. V. Löhneysen, *Phys. Rev. B* **2007**, *75*, 144402.
- [14] M. Csontos, G. Mihály, B. Jankó, T. Wojtowicz, X. Liu, J. K. Furdyna, *Nat. Mater.* **2005**, *4*, 447.
- [15] G. Shirane, C. W. Chen, P. A. Flinn, R. Nathans, *Phys. Rev.* **1963**, *131*, 183.
- [16] S. O. Mariager, F. Pressacco, G. Ingold, A. Caviezel, E. Möhr-Vorobeva, P. Beaud, S. L. Johnson, C. J. Milne, E. Mancini, S. Moyerman, E. E. Fullerton, R. Feidenhans'l, C. H. Back, C. Quitmann, *Phys. Rev. Lett.* **2012**, *108*, 087201.
- [17] J. Železný, P. Wadley, K. Olejník, A. Hoffmann, H. Ohno, *Nat. Phys.* **2018**, *14*, 220.
- [18] X. Marti, I. Fina, C. Frontera, J. Liu, P. Wadley, Q. He, R. J. Paull, J. D. Clarkson, J. Kudrnovský, I. Turek, J. Kuneš, D. Yi, J.-H. Chu, C. T. Nelson, L. You, E. Arenholz, S. Salahuddin, J. Fontcuberta, T. Jungwirth, R. Ramesh, *Nat. Mater.* **2014**, *13*, 367.
- [19] B. R. Mcgrath, R. E. Camley, K. L. Livesey, *Phys. Rev. B* **2020**, *101*, 014444.
- [20] L. I. Vinokurova, A. V. Vlasov, M. Pardavi-Horváth, *Phys. Status Solidi B* **1976**, *78*, 353.
- [21] J. B. Staunton, R. Banerjee, M. dos Santos Dias, A. Deak, L. Szunyogh, *Phys. Rev. B* **2014**, *89*, 054427.
- [22] F. Pressacco, D. Sangalli, V. Uhlíř, D. Kutnyakhov, J. A. Arregi, S. Y. Agustsson, G. Brenner, H. Redlin, M. Heber, D. Vasilyev, J. Demsar, G. Schönhense, M. Gatti, A. Marini, W. Wurth, F. Sirotti, *Nat. Commun.* **2021**, *12*, 5088.
- [23] R. O. Cherifi, V. Ivanovskaya, L. C. Phillips, A. Zobelli, I. C. Infante, E. Jacquet, V. Garcia, S. Fusil, P. R. Briddon, N. Guiblin, A. Mougín, A. A. Únal, F. Kronast, S. Valencia, B. Dkhil, A. Barthélémy, M. Bibes, *Nat. Mater.* **2014**, *13*, 345.
- [24] A. Hillion, A. Cavallin, S. Vlaic, A. Tamion, F. Tournus, G. Khadra, J. Dreiser, C. Piamonteze, F. Nolting, S. Rusponi, K. Sato, T. J. Konno, O. Proux, V. Dupuis, H. Brune, *Phys. Rev. Lett.* **2013**, *110*, 087207.
- [25] S. Lounis, M. Benakki, C. Demangeat, *Phys. Rev. B* **2003**, *67*, 094432.
- [26] C. C. Chao, P. Duwez, C. C. Tsuei, *J. Appl. Phys.* **1971**, *42*, 4282.
- [27] R. Witte, R. Kruk, M. E. Gruner, R. A. Brand, D. Wang, S. Schlabach, A. Beck, V. Provenzano, R. Pentcheva, H. Wende, H. Hahn, *Phys. Rev. B* **2016**, *93*, 104416.
- [28] B. Eggert, A. Schmeink, J. Lill, M. O. Liedke, U. Kentsch, M. Butterling, A. Wagner, S. Pascarelli, K. Potzger, J. Lindner, T. Thomson, J. Fassbender, K. Ollefs, W. Keune, R. Bali, H. Wende, *RSC Adv.* **2020**, *10*, 14386.
- [29] K. Sumiyama, M. Shiga, Y. Nakamura, *Phys. Status Solidi A* **1972**, *13*, K75.
- [30] G. Filoti, V. Kuncsea, E. Navarro, A. Hernando, M. Rosenberg, *J. Alloys Compd.* **1998**, *278*, 60.
- [31] V. Kuncser, M. Rosenberg, G. Principi, U. Russo, A. Hernando, E. Navarro, G. Filoti, *J. Alloys Compd.* **2000**, *308*, 21.

- [32] J. Erlebacher, M. J. Aziz, A. Karma, N. Dimitrov, K. Sieradzki, *Nature* **2001**, 410, 450.
- [33] I. Mccue, E. Benn, B. Gaskey, J. Erlebacher, *Annu. Rev. Mater. Res.* **2016**, 46, 263.
- [34] J. Weissmüller, R. N. Viswanath, D. Kramer, P. Zimmer, R. Würschum, H. Gleiter, *Science* **2003**, 300, 312.
- [35] J. Weissmüller, J. W. Cahn, *Acta Mater.* **1997**, 45, 1899.
- [36] J. Weissmüller, H.-L. Duan, D. Farkas, *Acta Mater.* **2010**, 58, 1.
- [37] X.-L. Ye, N. Lu, X.-J. Li, K. Du, J. Tan, H.-J. Jin, *J. Electrochem. Soc.* **2014**, 161, C517.
- [38] M. Graf, B.-N. D. Ngô, J. Weissmüller, J. Markmann, *Phys. Rev. Mater.* **2017**, 1, 076003.
- [39] B. E. Warren, *X-Ray Diffraction*, Dover Publications, Inc., Mineola, NY, USA **1990**.
- [40] W. F. Brown, *Phys. Rev.* **1963**, 130, 1319.
- [41] S. Süllo, G. J. Nieuwenhuys, A. A. Menovsky, J. A. Mydosh, S. A. M. Mentink, T. E. Mason, W. J. L. Buyers, *Phys. Rev. Lett.* **1997**, 78, 354.
- [42] J. A. Mydosh, *Rep. Prog. Phys.* **2015**, 78, 052501.
- [43] J. Lauer, W. Keune, *Phys. Rev. Lett.* **1982**, 48, 1850.
- [44] H. Ebert, D. Ködderitzsch, J. Minár, *Rep. Prog. Phys.* **2011**, 74, 096501.
- [45] J. P. Perdew, K. Burke, M. Ernzerhof, *Phys. Rev. Lett.* **1996**, 77, 3865.
- [46] B. L. Gyorffy, A. J. Pindor, J. Staunton, G. M. Stocks, H. Winter, *J. Phys. F* **1985**, 15, 1337.
- [47] R. D. Ellerbrock, A. Fuest, A. Schatz, W. Keune, R. A. Brand, *Phys. Rev. Lett.* **1994**, 74, 3053.
- [48] D. J. Keavney, D. F. Storm, J. W. Freeland, I. L. Grigorov, J. C. Walker, *Phys. Rev. Lett.* **1995**, 74, 4531.
- [49] X.-L. Ye, H.-J. Jin, *Appl. Phys. Lett.* **2013**, 103, 201912.
- [50] L. Lührs, B. Zandersons, N. Huber, J. Weissmüller, *Nano Lett.* **2017**, 17, 6258.
- [51] N. Huber, R. N. Viswanath, N. Mameka, J. Markmann, J. Weißmüller, *Acta Mater.* **2014**, 67, 252.
- [52] C. Mahr, K. Müller-Caspary, M. Graf, A. Lackmann, T. Grieb, M. Schowalter, F. F. Krause, T. Mehrtens, A. Wittstock, J. Weissmüller, A. Rosenauer, *Mater. Res. Lett.* **2018**, 6, 84.
- [53] D. W. Boukhvalov, Y. N. Gornostyrev, M. I. Katsnelson, A. I. Lichtenstein, *Phys. Rev. Lett.* **2007**, 99, 247205.
- [54] T. Yokota, *Phys. Rev. E* **2014**, 89, 012128.
- [55] J. Kieffer, V. Valls, T. Vincent, J. P. Wright, R. Pandolfi, G. Ashiotis, B. Faure, C. J. Wrigh, F. Plaswig, S. Neher, G. Flucke, A. Hov, silx-kit/pyFAI: PyFAI v0.20.0, <https://doi.org/10.5281/zenodo.832896>, (accessed: May 2021).
- [56] S. Martin, C. Ullrich, D. Šimek, U. Martin, D. Rafaja, *J. Appl. Cryst.* **2011**, 44, 779.
- [57] W. H. Butler, *Phys. Rev. B* **1985**, 31, 3260.